Biosensors and Bioelectronics 140 (2019) 111330

Contents lists available at ScienceDirect

Biosensors and Bioelectronics

journal homepage: www.elsevier.com/locate/bios

Facile preparation of molybdenum carbide (Mo_2C) nanoparticles and its effective utilization in electrochemical sensing of folic acid via imprinting

Sajjad Hussain[a,b,1], Shabi Abbas Zaidi[c,**,1], Dhanasekaran Vikraman[d], Hyun-Seok Kim[d], Jongwan Jung[a,b,*]

[a] Graphene Research Institute, Sejong University, Seoul, 05006, Republic of Korea
[b] Department of Nano and Advanced Materials Engineering, Sejong University, Seoul, 05006, Republic of Korea
[c] Department of Chemistry, Kwangwoon University, 20 Kwangwoon-ro, Nowon-Gu, Seoul, 01897, Republic of Korea
[d] Division of Electronics and Electrical Engineering, Dongguk University-Seoul, Seoul, 04620, Republic of Korea

ARTICLE INFO

Keywords:
Mo_2C nanoparticles
Chemical reduction
Folic acid
Molecular imprinting polymer
Pyrrole

ABSTRACT

Herein, we propose a facile chemical reduction method to synthesize the molybdenum carbide (Mo_2C) nanoparticles and its application for the electrochemical detection of folic acid (FA) through imprinting technique. Raman scattering, photoelectron spectroscopy and electron microscopy techniques were employed to study the properties of Mo_2C nanoparticles. FA imprinting was carried out in the presence of pyrrole monomer over Mo_2C modified glassy carbon electrode (GCE). The proposed sensor showed the detection behavior for wide range of FA concentrations from 0.01 μM to 120 μM with an excellent LOD value of 4 nM and good selectivity toward FA as compared to other co-existing species in real samples. The fabricated MIP-Mo_2C/GCE sensors were able to be replicated with ~1.9% RSD, and their reproduced sensor offered good repeatability (RSD; 1.6%) and stability.

1. Introduction

Molybdenum carbide (Mo_2C), an emerging member of MXene group, has attracted considerable attention in recent time as a new class of highly robust 2D materials for potential applications in energy storage (Liu et al., 2015; Xu et al., 2015). Mo_2C possesses attractive properties such as high surface area, high theoretical capacity (600–1000 mA h g^{-1}), good electrical conductivity (~1.0×10^2 S cm^{-1}), and high thermal stability (Chen et al., 2017; Zhang et al., 2014; Zhu et al., 2015). Like other transition metal carbides, Mo_2C has been effectively utilized in electrochemical energy storage (Xiao et al., 2016), gas sensing (Cho et al., 2018), hydrogen evolution reaction (HER) (Kumar et al., 2017), catalytic conversion (Xiong et al., 2014), and electrochemical immunosensing (Zhai et al., 2016).

A key issue is the development of Mo_2C material by the controlled synthesis process. Generally, Mo_2C is prepared by carburization of metals with graphitic carbon at high temperature (> 1000 °C) due to its high melting point or by chemical etching of layered Mo-containing ternary phases (Halim et al., 2016; Naguib et al., 2015). These processes can lead the aggregation and/or disproportionate growth of Mo_2C by forming large grains with low specific surface area as well as poor density of active sites and porous nanostructure, which is not beneficial for its further applications. Recently synthesis of transition metal dichalcogenides and various functionalized 2D multi-layered metal carbides/carbonitrides (MXene) including Mo_2C have been carried out by selective etching with concentrated HF or a solution of LiF and HCl (Ng et al., 2017; Yuan et al., 2018). However, Mo_2C prepared by these methods suffers severe structural defects due to bonding formation with residue such as oxygen (= O), hydroxyl (-OH) or fluorine (-F) functional groups which are attached to the surface of M atoms during the surface-terminating etching process (Anasori et al., 2017; Halim et al., 2016; Yuan et al., 2018). Hence, the synthesis of well dispersed, high purity, controllable and electrochemically accessible Mo_2C nanoparticles is still challenging due to the lack of scalable preparation method. In addition, the simple route of preparation is prerequisite. In this work, we described a facile chemical reduction method to synthesize the Mo_2C nanoparticles and showed its effective application in electrochemical sensing of folic acid (FA).

FA, a water soluble vitamin, is considered one of the most vital constituent of our food supplements as its deficiency causes many detrimental health complications including psychosis and

* Corresponding author. Graphene Research Institute, Sejong University, Seoul, 05006, Republic of Korea.
** Corresponding author.
E-mail addresses: shabizaidi79@gmail.com (S.A. Zaidi), jwjung@sejong.ac.kr (J. Jung).
[1] Authors have equally contributed.

https://doi.org/10.1016/j.bios.2019.111330
Received 7 March 2019; Received in revised form 13 May 2019; Accepted 15 May 2019
Available online 18 May 2019
0956-5663/

cardiovascular problems, carcinogenic symptoms, neural tube defects in newborns, gigantocytic anemia, leucopoenia, and devolution of mentality. Hence, its analysis from the clinical point of view is highly demanded. Electrochemical methods have been reported for reliable determination of FA(Arvand and Dehsaraei, 2013; Lavanya et al., 2016). However, the accurate determination of FA in the presence of other electrochemical active compounds in a complex real sample poses serious challenges, which led us to exploit the modification of electrode material with tailor-made selectivity of molecularly imprinted polymers (MIPs). Molecular imprinting technique is considered as one of the most useful preparation strategies to obtain highly selective polymeric materials (Zaidi, 2013, 2018). MIP offers great selectivity and considerable promise for applications in clinical analysis, medical diagnostics, environmental monitoring and drug delivery (Pan et al., 2017a; Piletsky et al., 2006; Zaidi, 2016, 2017; Zaidi et al., 2011).

To the best of our knowledge, there is no report about Mo_2C as the electrode component for electrochemical sensing of FA via MIP. We have successfully synthesized Mo_2C nanoparticles through a facile chemical reduction procedure and employed the efficient electron facilitating and catalytic properties of Mo_2C in electrochemical sensing of FA via MIP. FA was imprinted in the presence of pyrrole over Mo_2C modified glassy carbon electrode (GCE) by electropolymerization. The as-proposed MIP sensor exhibited high selectivity, sensitivity, and accurate determination of FA.

2. Material and method

2.1. Materials

Commercial - 325 mesh Mo_2C powder (99.5% purity), folic acid (FA), pyrrole, uric acid (UA), ascorbic acid (AA), dopamine (DA), glucose, progesterone (Prg), cortisol, lactate, and all other reagents were purchased from Sigma-Aldrich. PBS buffer (0.1 M, pH-6.5) was prepared by dissolving sodium phosphate monobasic monohydrate ($NaH_2PO_4.H_2O$) and sodium phosphate dibasic dihydrate ($Na_2HPO_4.2H_2O$) and sodium chloride (NaCl) in DI water. The 1 mM $K_3[Fe(CN)_6]^{3-/4-}$ (1:1) solution containing 0.1 M potassium chloride (KCl) was prepared as a redox probe for cyclic voltammetry (CV) analysis.

2.2. Synthesis of Mo_2C nanoparticles

Initially, Mo_2C powder (1 g) was well dispersed in a beaker with 50 mL of ethanol. Next, the black mixture was stirred under room temperature for 3 h for the homogeneous solution. After stirring, 25 mL of NH_3 was mixed and then subjected to vigorous stirring at 85 °C for 5 h. After the solution mixture reached to room temperature, the sediment was extracted by centrifuge as black powder and then cleansed with DI water several times to remove residues. Finally, the black powder was transferred to a quartz tube and was kept in the center of the quartz tube for thermal annealing at 800 °C for 3 h in the gas mixture of Ar, H_2 (80 sccm) and CH_4 gas (50 sccm). After the reaction, the tube was cooled to room temperature in Ar gas environment, and the final product of Mo_2C nanoparticles was collected.

2.3. Sensor preparation

Firstly, the cleaned GCEs were electrochemically activated via 10 cyclic potential sweeps in 0.01 M H_2SO_4 electrolyte at a scan rate of 100 mV s^{-1} in the range of −1.0–1.0 V. Then, 2 successive aliquots of 1–2 μL freshly prepared Mo_2C nanoparticles dispersion (1.5 mg/mL aqueous dispersion) was dropped over the activated area of GCE and dried at room temperature. For the FA MIP, the Mo_2C/GCE was immersed in a solution mixture of 0.0025 M FA and 0.01 M pyrrole (pH; 7.2) and 0.1 M $LiClO_4$. The FA molecules were extracted by dipping the as-fabricated sensor in the solution of ethanol and acetic acid (90:10 v/v%) under mild stirring. The complete removal of FA molecules from the MIP polymer matrix was confirmed through CV. The similar protocol was followed to prepare Non-imprinted polymer (NIP)–Mo_2C/GCE sensor without inclusion of FA in the electropolymerization solution. In addition, MIP/GCE and NIP/GCE were fabricated similar to MIP-Mo_2C/GCE and NIP–Mo_2C/GCE, respectively without drop of Mo_2C.

2.4. Material characterization

Powder X-ray diffraction (XRD) analysis was performed to check the crystallinity of the samples by Rigaku Ultima IV diffractometer at room temperature with Cu-Kα radiation (0.154 nm) using 5°/m scan rate, 40 kV voltage and 40 mA current in a scanning range of 10–80° (2θ). Synthesized Mo_2C nanoparticles were analyzed by Raman spectroscopy (Renishaw invia RE04, 512 nm Ar laser) with a spot size of 1 μm and a scan speed of 30 s. X-ray photoelectron spectroscopy (XPS) (PHI 5000 Versa Probe, 25 W Al Kα, 6.7 × 10-8 Pa) was used to confirm the chemical composition. Transmission electron microscopy (TEM) samples were prepared using lacey-carbon Cu grid. The atomic structure of Mo_2C nanoparticles was characterized by a JEOL-2010F TEM with an accelerating voltage of 200 keV with the support of Gatan Digital Micrograph software (version 3.0). The specific surface area of Mo_2C catalysts was measured by nitrogen sorption measurement at 77 K on a 3Flex surface characterization analyzer (Micromeritics, USA).

The electrochemical studies including electrochemical impedance analysis (EIS) were performed using a potentiostat (CH instruments model 600B) with three electrode set-up, in which Pt wire, Ag/AgCl, and fabricated sensors (MIP-Mo_2C/GCE, NIP– Mo_2C/GCE, MIP/GCE and NIP/GCE) are used as the counter, reference, and working electrodes, respectively. For the electrochemical studies, a buffer solution containing 0.1 M KCl in 0.1 M PBS of pH 6.5 was employed with a scan rate of 100 mV s^{-1}. The equivalent circuit and fitted results were obtained with ZSimpWin software (Princeton Applied Research, Massachusetts, USA).

3. Results and discussion

Mo_2C nanostructure catalyst is successfully synthesized by chemical reduction process as elaborated in the experimental section. Schematic synthesis process of Mo_2C nanostructure catalyst is illustrated in Fig. 1.

3.1. Structural and morphological properties of Mo_2C nanoparticles

To investigate the insights in the bonding structure of commercial Mo_2C and chemically reduced Mo_2C, Raman spectroscopy was conducted. No distinct characteristic peaks were observed for commercial Mo_2C (Fig. 2(a): black line). For chemically reduced Mo_2C, Raman spectrum displays three characteristic bands of Mo_2C at ~660, ~818, and ~989 cm^{-1}, as well as the sp^2-bonded graphitic carbon related D and G bands at ~1345 and ~1583 cm^{-1}, respectively (Fig. 2(a): red line) (Huang et al., 2016; Wang et al., 2017). The intensity ratio of D to G-band (I_D/I_G) is a crucial factor to assess the nature of the graphitization (Li et al., 2016). The observed intensity ratio of I_D/I_G is ~0.89 for the chemically reduced Mo_2C nanoparticles which is consistent with well-ordered graphene layers (Li et al., 2016; Lv et al., 2017; Pu et al., 2016). The crystalline phases of commercial Mo_2C and chemically reduced Mo_2C are revealed by XRD as shown in Fig. 2(b). XRD peaks at 34.6, 38.0, 39.4, 52.3, 61.7, 69.9, 74.7 and 75.8° are well indexed to the (100), (002), (101), (102), (110), (103), (112) and (201) planes, respectively related to β-Mo_2C (JCPDS card no. 35–0787) (Tang et al. 2015a, 2015b; Wang et al., 2017). The peak intensities are higher for the chemically reduced Mo_2C compared with the commercial Mo_2C. To further confirm the composition of the chemically reduced Mo_2C, XPS analysis was carried out. The survey spectrum shows the characteristic signals of Mo and C (Fig. S1). Fig. 2(c) shows the deconvoluted high-

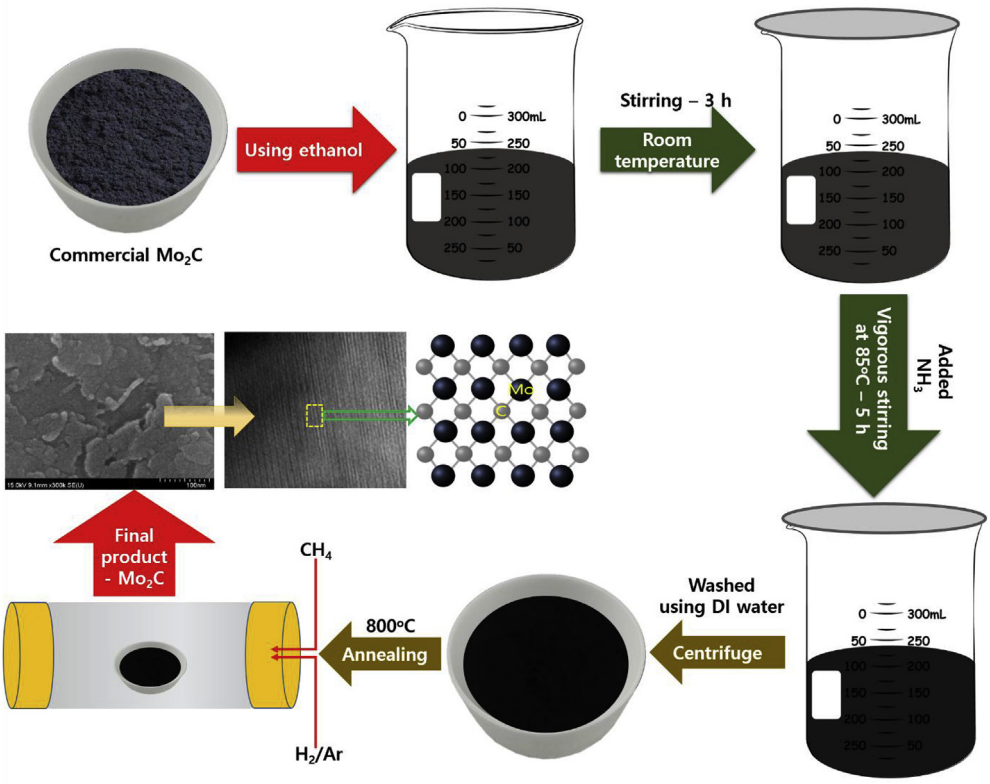

Fig. 1. Illustration of synthesis of Mo_2C nanoparticles.

resolution profile for Mo 3d binding energy. The couple of peaks located at 229.5 and 233.0 eV and at 232.7 and 235.8 eV were assigned to Mo^{4+} and Mo^{6+}, respectively, indicating partial oxidation on the surface owing to exposure to the ambient environment (Fan et al., 2018; Pan et al., 2017b; Qamar et al., 2016). Fig. 2(d) displays C 1s spectrum with the characteristic peak of graphitic carbon at 284.6 eV and C–O group at 285.5 eV for the chemically reduced Mo_2C (Qamar et al., 2016; Wang et al., 2017).

The morphology of the chemically reduced Mo_2C was analyzed by FESEM and TEM. Fig. 3(a–b) shows the low and higher magnification FESEM images for the chemically reduced Mo_2C. The elemental composition of the chemically reduced Mo_2C nanoparticles was determined by energy-dispersive spectroscopy (EDS) as presented in Fig. S2. Atomic percentages of Mo and C are 72.7 and 27.3%, respectively for the chemically reduced Mo_2C nanoparticles. EDS elemental mapping (Figs. S3a–c) indicates that the Mo, and C atoms are uniformly distributed, which verifies the homogeneous distribution on Mo_2C nanoparticles. TEM images (Fig. 3(c-d)) demonstrate the well-structured and layered Mo_2C nanoparticle. The inverse FFT fringes with interplanar distance of 0.23 nm is observed, which is corresponding to the (101) crystal plane of β-Mo_2C (Fig. 3(e)). TEM-EDS mapping indicates the coexistence of Mo and C elements in the whole Mo_2C as shown in Fig. S4.

Brunauer-Emmett-Teller (BET) method was applied to measure the specific surface area and porosity. Fig. S5a displays nitrogen adsorption–desorption isotherms plot for the chemically reduced Mo_2C. The chemically reduced Mo_2C shows a specific surface area of 0.91 $m^2 g^{-1}$, which is consistent with commercial Mo_2C (0.86 $m^2 g^{-1}$) (Gao et al., 2014). The pore diameter against pore volume spectrum (Fig. S5b) predicts the mesoporous structure of chemically reduced Mo_2C with the pore diameter of 14.9 nm and the pore volume of 0.003 $cm^3 g^{-1}$. Electrical conductivities of all samples were measured by four pin probe method. The values of commercial and chemically reduced Mo_2C were ~40 and 90 S/cm, respectively.

3.2. Electropolymerization of folic acid with pyrrole

To create the NIP film and FA MIP film, Mo_2C/GCEs were immersed in pyrrole monomer solution without and with FA, respectively, and electropolymerization was carried out as shown in Fig. S6. Fig. S6(a) shows the growth of polymer NIP film. When the electropolymerization process takes place in the presence of FA with pyrrole monomer solution to achieve MIP film, the effect of FA on the electropolymerization of pyrrole is clearly exposed as seen in Fig. S6(b). The oxidation peak potential of polypyrrole is shifted to more anodic potential, and a new peak is appeared at ~0.67 V in the presence of FA, indicating that the template is becoming a part of the polymeric chain. However, the sharp peak disappears after few scans owing to mutual interaction of FA with the polypyrrole and thereby continues the film growth. It can be assumed that strong interaction of acidic functionalities of FA and basic functional groups of pyrrole created a robust MIP film. The possible interactions between template and functional monomer during MIP synthesis are provided in Fig. S7.

3.3. Electrochemical characterization of various modified sensor

A solution comprised of 1 mM $K_3[Fe(CN)_6]^{3-/4-}$ and 0.1 M KCl (1:1) was used to study the electrochemical behavior of various modified sensors via CV technique at a scan rate of 100 mV s^{-1} as shown in Fig. 4 (a). The bare GCE exhibits a well reversible redox peak with satisfactory peak separation of ~150 mV which decreases to nearly 100 mV after its modification with Mo_2C which enhanced the current response considerably. It is revealed that Mo_2C is catalytically active and facilitates the electron transfer owing to its good electrical conductivity. After the formation of MIP over Mo_2C/GCE, the peak currents reduce significantly with the sharp increase of peak separation, which verifies the fact that MIP was successfully formed and $K_3[Fe(CN)_6]$ molecules were not able to infiltrate the polymer matrix. After the removal of FA molecules, the signal response increases again with the decrease of peak separation, supporting the creation of FA cavities

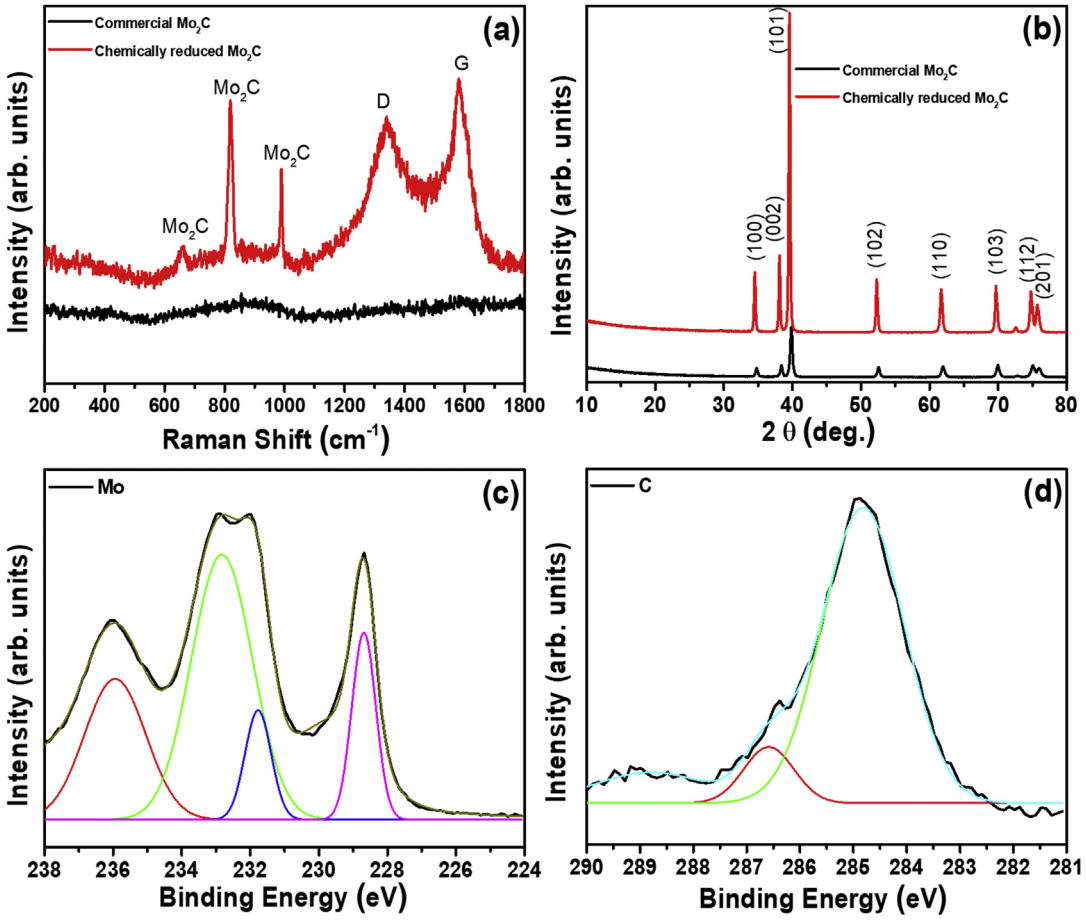

Fig. 2. Structural properties of Mo_2C nanoparticles. **(a)** XRD and **(b)** Raman spectra for commercial and chemically reduced Mo_2C; XPS spectra for chemically reduced Mo_2C nanoparticles with their de-convoluted curves **(c)** Mo 3d and **(d)** C 1s.

which are now accessible by $K_3[Fe(CN)_6]$ molecules. It is worth noting that the current response of MIP-Mo_2C/GCE after template removal is still inferior to that of Mo_2C/GCE due to the formation of MIP layer. In the case of NIP–Mo_2C/GCE, the $K_3[Fe(CN)_6]$ redox response is marginal with high peak redox separation due to the non-availability of cavities and negligible porosity. In order to see the effect of Mo_2C, control experiments were also carried out by modifying the GCEs with MIP and NIP films as shown in Fig. S8. It can be concluded that although MIP/GCE bears available cavities for redox probe molecules penetration, its signal intensity is significantly low due to the absence of Mo_2C. On the other hand, response of NIP/GCE is negligible owing to its non-availability of cavities. The electrochemical behaviors of these sensors are well supported by EIS results in Fig. 4(b). The corresponding fitted curves from the equivalent circuit model of the inset are plotted with cyan color (Fig. 4(b)). Nyquist plot consists of two portions; the semi-circular section at high frequencies, related to R_{ct} and a linear portion at low frequencies, which is related to diffusion limited processes in solution. In the equivalent circuit, R_1 and W_1 are the resistances of the solution and the Warburg impedance, respectively. R_{ct}, which was caused by charge transfer reactions (Faraday processes) and the diffusion of ions from the electrolyte to the interface, and the interfacial double layer capacitance (C_{dl}) was treated as the constant phase element. The fitted R_1, and R_{ct} values are provided in Table S1. The R_{ct} of Mo_2C/GCE, and bare GCE sensor are ~309 Ω, and 2400 Ω, respectively. The low R_{ct} of the Mo_2C/GCE can be attributed to the favorable charge transfer and high electrical conductivity of Mo_2C nanoparticles. On the other hand, MIP-Mo_2C/GCE with FA molecules offers wider semi-circle region of ~2012 Ω which is again reduced to ~1431 Ω after the removal of FA molecules from the MIP layer. The highest charge transfer resistance of ~2682 Ω was obtained for NIP–Mo_2C/GCE.

Fig. 4(c) demonstrates the electrochemical behavior of FA by using MIP-Mo_2C/GCE and NIP–Mo_2C/GCE sensors after incubating the sensors in FA solution. The inset of Fig. 4(c) shows the reaction mechanism of FA oxidation. A very weak oxidation peak is shown for bare GCE, whereas the oxidation peak increases when Mo_2C/GCE sensor is employed, pointing that Mo_2C nanoparticles exhibit some catalytic effects and its high electrical conductivity promotes electron transfer. For MIP-Mo_2C/GCE sensor, the oxidation current of FA is decreased due to the non-conductivity of MIP film and the peak is shifted to positive potential which is in agreement with other results (Fig. 4(a) and (b)). A negligible response of FA was shown by NIP–Mo_2C/GCE sensor, which authenticates that there are few cavities available for FA accumulation. This negligible response may be due to few physically adsorbed FA molecules over NIP surface. From the observed results, it can be concluded that Mo_2C nanoparticles act as a rapid electron facilitator and provide the better MIP-Mo_2C/GCE sensor. Additionally, FA molecules are trapped in their complementary cavities and then oxidized once the potential is applied across the MIP-Mo_2C/GCE sensor.

3.4. Optimization of various experimental factors

In order to achieve the maximum efficiency from as-synthesized MIP-Mo_2C/GCE sensor, several experimental parameters including the loading of Mo_2C over GCE, pH of buffer and sensor incubation time in FA solution were optimized. Fig. S9(a) displays the effects of different loading mass of Mo_2C on GCE and it shows that 1.5 mg/mL of Mo_2C loading offered the highest current response. Lower loading (< 1.5 mg/

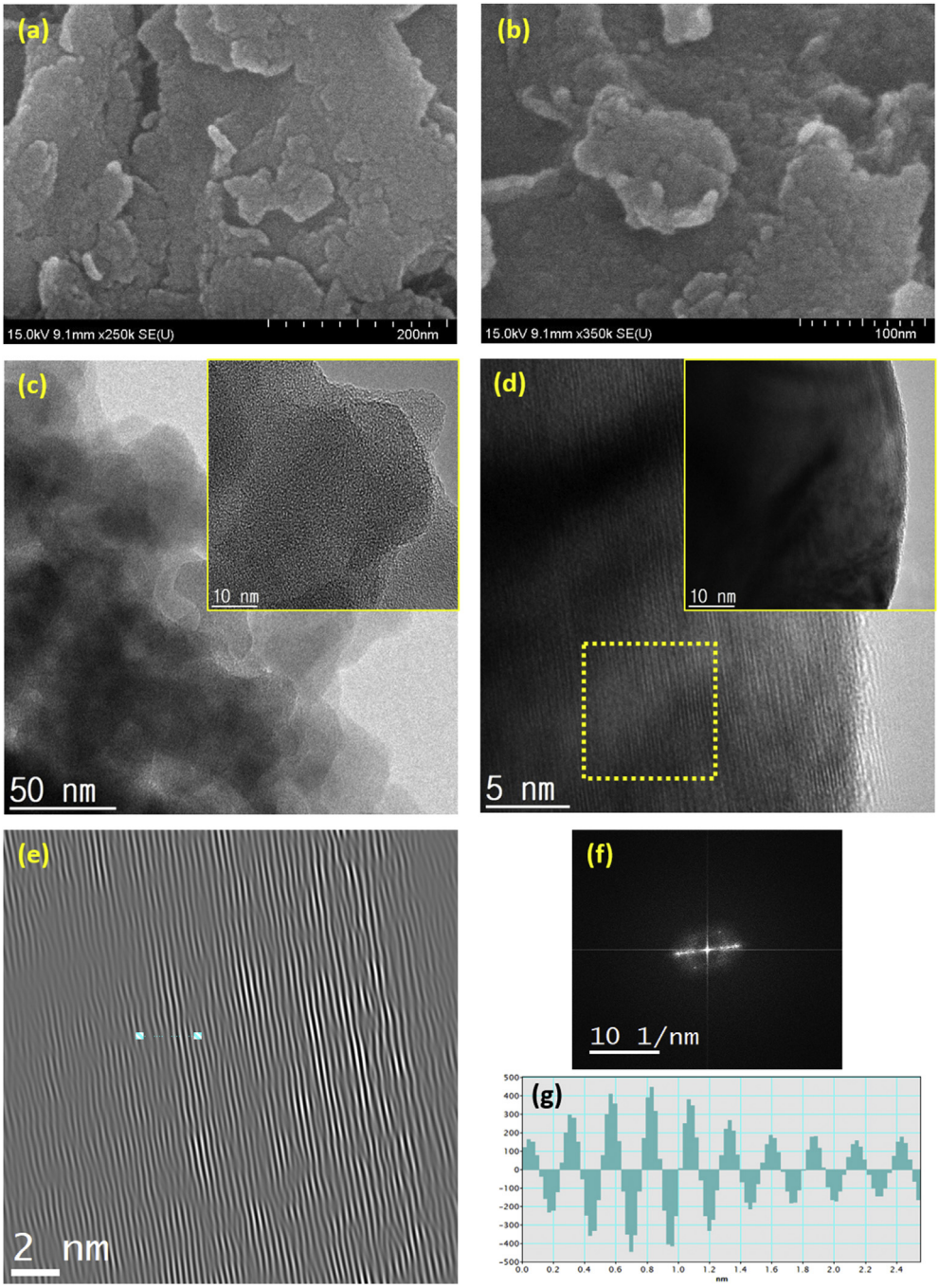

Fig. 3. Surface properties of Mo_2C nanoparticles. **(a–b)** SEM images at different magnifications; **(c–g)** HRTEM images of Mo_2C. **(c)** Low magnification image (inset - higher magnification). **(d)** Layered structure of Mo_2C HRTEM image (inset – corresponding portion of low magnification image). **(e)** Inverse FFT pattern for yellow line indicated portion of (d) by point mask mode and their **(f)** FFT and **(g)** phase profile spectrum for cyan color lined portion of (e). (For interpretation of the references to color in this figure legend, the reader is referred to the Web version of this article.)

mL) may not be sufficient to effectively facilitate the electron transfer, whereas higher (> 1.5 mg/mL) loading may build a thicker layer of Mo_2C, thus hinders the electron transfer from MIP to electrode surface. The number of electropolymerization cycle is also a key parameter for MIP-Mo_2C/GCE sensitivity as shown in Fig. S9(b). The current response increases up to 10 cycles, probably due to FA imprinted cavities on MIP-Mo_2C/GCE. Whereas beyond the 10 cycles, current is decreased considerably, maybe due to the increased filled imprinted cavities, which make FA molecules immovable. The different pH was examined and better response was obtained from pH 6.5 as depicted in Fig. S9(c). For the role of incubation time, the prepared MIP-Mo_2C/GCE sensor was immersed in FA solution under mild stirring. Fig. S9(d) shows current response on different incubation time for MIP-Mo_2C/GCE sensor. The sensor electrode incubated for 4 m produced the highest current response and then after 4 m, the current response was saturated probably due to the highly occupied FA cavities.

3.5. Calibration curve and analytical applications

For the calibration study and LOD calculation, current versus concentration of FA was recorded using MIP-Mo_2C/GCE and NIP–Mo_2C/GCE via the differential pulse voltammogram (DPV) technique under

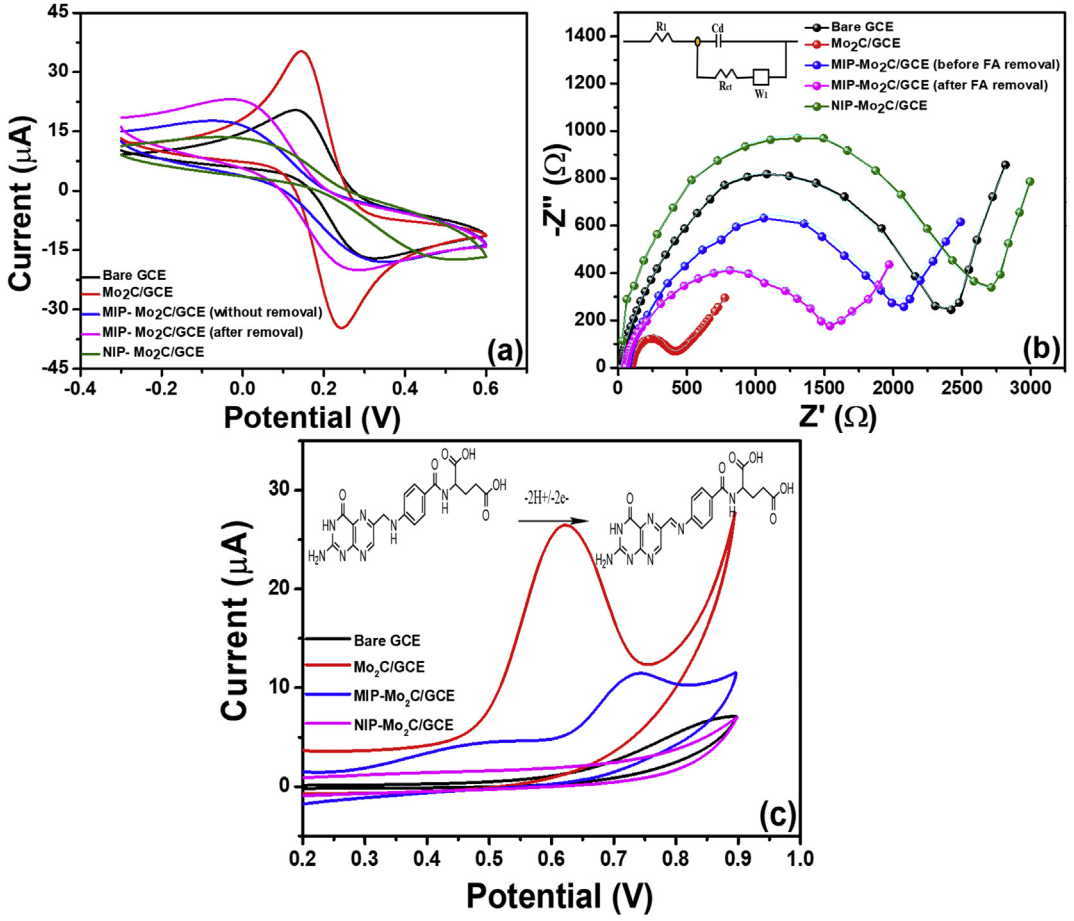

Fig. 4. (a) Cyclic voltammograms of bare GCE, Mo_2C/GCE, and MIP- Mo_2C/GCE (without template removal), MIP-rGO/GCE (after template removal), and NIP–Mo_2C/GCE in 1 mM $[Fe(CN)6]^{3-/4-}$containing 0.01 M KCl (1:1) solution at a scan rate of 100 mV s^{-1}. (b) Nyquist plots and their fitted curves with cyan color for various modified GCEs; experimental parameters: 0.1 M PBS (pH-6.5) with 0.01 M $K_3[Fe(CN)_6]^{3-/4-}$, frequency range, 100 mHz–100 kHz; potential, 0.2 V; and AC voltage, 4 mV. (c) Cyclic voltammograms study of various modified GCEs in FA solution of 0.1 M KCl and 0.1 M PBS (pH-6.5) at a scan rate of 100 mV s^{-1}. Inset - reaction mechanism of FA oxidation. (For interpretation of the references to color in this figure legend, the reader is referred to the Web version of this article.)

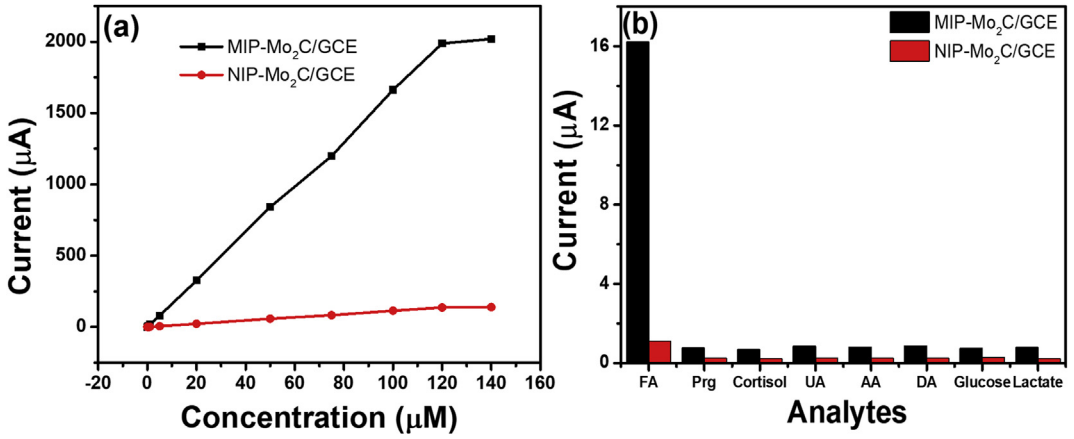

Fig. 5. Calibration curve obtained after DPV analysis of increasing concentration of FA between 0.01 μM and 140 μM, and (b) selectivity of FA molecules (1 μM) in the presence of other interfering compounds (each 50 μM) using MIP- Mo_2C/GCE and NIP– Mo_2C/GCE sensors (mean results of triplicate (n = 4)). Experimental parameters: 0.1 M KCl and 0.1 M PBS (pH-6.5) with a scan rate: 0.1 V s^{-1}.

the optimized conditions. Fig. 5(a) indicates that the oxidation current increases rapidly with the increase of FA concentration from 0.01 μM to 120 μM with a regression coefficient (R^2) value of 0.996 for MIP-Mo_2C/GCE. The estimated regression coefficient for NIP–Mo_2C/GCE sensor is 0.982. From the calibration plot, the LOD for FA is calculated to be 4 nM (S/N = 3, RSD < 5%) based on four measurements for MIP-Mo_2C/GCE. An imprinting factor (I_{MIP}/I_{NIP}) is found to be 14.6.

One of the most lucrative features of MIP is its tailor-made selectivity. The selectivity experiment was carried out with MIP-Mo_2C/GCE and NIP–Mo_2C/GCE sensors by acquiring the DPV responses of 1 μM FA in the presence of each 50 μM of other interfering compounds (i.e. Prg, cortisol, lactate, UA, AA, DA, and glucose) in Fig. 5 (b). The

Table 1
Analysis of FA in real samples using MIP-Mo_2C/GCE.

Sample	Measured/ made (μM)	Added (μM)	Expected (μM)	Found[c] (μM)	Recovery (%)	RSD (%)
Pharmaceutical[a]						
1	90	10	100	98.75	98.75	3.35
2	25	10	35	35.5	101.4	4.74
3	11	10	21	20.9	99.5	1.50
4	5.5	10	15.5	15	96.77	3.96
Serum[b]						
1	-[b]	50	50	50.25	100.5	3.00
2	–	4	4	4.00	100.0	3.54
3	–	0.5	0.5	0.49	98.0	5.65
4	–	0.05	0.05	0.048	96.0	5.00

[a] Original concentration is 1 mg/mL which is diluted to acquire the desired concentrations
[b] No trace of FA was found
[c] n = 4 (average of four replicate assays)

results show that even the 50 times higher concentration of other interfering compounds does not hinder the detection of FA molecules. On the other hand, significantly low oxidation current for FA is observed by NIP–Mo_2C/GCE. And even lower current detection for other molecules by NIP–Mo_2C/GCE sensor may be arisen due to physical adsorption of few molecules of FA over NIP surface. The analytical applicability of proposed sensors was examined for the determination of FA in urine and ampoules. For the analysis, the different amount of FA was added in the urine and ampoules samples separately and recovery of FA was estimated. The sensor allowed the successful recognition with superb recoveries of FA in DPV analysis. Recoveries were found to lie in the range of 96–98% and 97–100.7% in urine and ampoules samples, respectively, which are under permissible relative standard deviation (RSD) limits (< 5%) as listed in Table 1.

3.6. Stability and reproducibility of the sensor

Our proposed sensor exhibited good repeatability, reproducibility and stability as shown in Fig. S10. For the repeatability test, the sensor currents were measured 6 times with the same MIP-Mo_2C/GCE in Fig. S10a, and it shows only 1.6% RSD. For the reproducibility test, 4 different of MIP-Mo_2C/GCE sensors were fabricated under same conditions (Fig. S10b). It shows 1.9% of RSD value. For the stability of sensor, the sensor showed no significant changes until 15 days. However, the sensitivity of FA detection decreased gradually after 15 days. The sensor detection capacity is reduced to less than 50% before 30 days but more than 50% after 35 days which may be attributed to the leaching and fouling of MIP-Mo_2C/GCE sensor (Fig. S10c). We think that due to the strong interaction between Mo_2C and MIP film, the stability is improved. Nevertheless, the proposed MIP-Mo_2C/GCE sensor results are comparable or better in terms of sensitivity and linear range of concentrations compared with earlier reported results as presented in Table S2 (Arvand and Dehsaraei, 2013; Jiang et al., 2009; Kanchana and Sekar, 2015; Lavanya et al., 2016). Hence, these results confirm that MIP can be utilized efficiently for the Mo_2C modified GCE for the recognition of FA.

4. Conclusions

In this work, we successfully synthesized Mo_2C nanoparticles via chemical reduction process and showed their effective application in the detection of FA via imprinting polymer preparation, for the first time. The prepared MIP-Mo_2C/GCE sensor showed high sensitivity and selectivity for FA due to the synergic effects from Mo_2C nanoparticles and imprinted cavities. The results suggest the potential of Mo_2C nanoparticles with the combination of polymer imprinting for the future sensor devices.

Declaration of interests

The authors declare that they have no known competing financial interests or personal relationships that could have appeared to influence the work reported in this paper.

CRediT authorship contribution statement

Sajjad Hussain: Methodology, Writing - original draft. **Shabi Abbas Zaidi:** Conceptualization, Formal analysis. **Dhanasekaran Vikraman:** Data curation, Investigation. **Hyun-Seok Kim:** Supervision, Validation. **Jongwan Jung:** Writing - review & editing, Supervision.

Acknowledgements

This research was supported by the Basic Science Research Program through the National Research Foundation of Korea, funded by the Ministry of Education (2015M3A7B7045194, 2017R1C1B5076952, and 2012R1A6A1029029), by the MOTIE (10052928) and the KSRC (Korea Semiconductor Research Consortium) support programs for the development of future semiconductor devices. This work was supported by the Korea Institute of Energy Technology Evaluation and Planning and the Ministry of Trade, Industry and Energy of the Republic of Korea (20172010106080). Shabi Abbas Zaidi is thankful to Kwangwoon University for research fund in 2019.

Appendix A. Supplementary data

Supplementary data to this article can be found online at https://doi.org/10.1016/j.bios.2019.111330.

References

Anasori, B., Lukatskaya, M.R., Gogotsi, Y., 2017. 2D metal carbides and nitrides (MXenes) for energy storage. Nature Reviews Materials 2 (2), 16098.
Arvand, M., Dehsaraei, M., 2013. A simple and efficient electrochemical sensor for folic acid determination in human blood plasma based on gold nanoparticles–modified carbon paste electrode. Mater. Sci. Eng. C 33 (6), 3474–3480.
Chen, J., Huang, Y., Zhao, F., Ye, H., Wang, Y., Zhou, J., Liu, Y., Li, Y., 2017. A hierarchical α-MoC 1 − x hybrid nanostructure for lithium-ion storage. J. Mater. Chem. 5 (17), 8125–8132.
Cho, S.-Y., Kim, J.Y., Kwon, O., Kim, J., Jung, H.-T., 2018. Molybdenum carbide chemical sensor with ultrahigh signal-to-noise ratio and ambient stability. J. Mater. Chem. 6, 23408–23416.
Fan, M., Zheng, Y., Li, A., Ma, Y., Huo, Q., Qiao, Z.A., Dai, S., 2018. Sprout-like growth of mesoporous Mo2C/NC nanonetworks as efficient electrocatalysts for hydrogen evolution. ChemCatChem 10 (3), 625–631.
Gao, Q., Zhao, X., Xiao, Y., Zhao, D., Cao, M., 2014. A mild route to mesoporous Mo2C–C hybrid nanospheres for high performance lithium-ion batteries. Nanoscale 6 (11), 6151–6157.
Halim, J., Kota, S., Lukatskaya, M.R., Naguib, M., Zhao, M.Q., Moon, E.J., Pitock, J., Nanda, J., May, S.J., Gogotsi, Y., 2016. Synthesis and characterization of 2D molybdenum carbide (MXene). Adv. Funct. Mater. 26 (18), 3118–3127.
Huang, Y., Gong, Q., Song, X., Feng, K., Nie, K., Zhao, F., Wang, Y., Zeng, M., Zhong, J., Li, Y., 2016. Mo2C nanoparticles dispersed on hierarchical carbon microflowers for efficient electrocatalytic hydrogen evolution. ACS Nano 10 (12), 11337–11343.
Jiang, X.-l., Li, R., Li, J., He, X., 2009. Electrochemical behavior and analytical determination of folic acid on carbon nanotube modified electrode. Russ. J. Electrochem. 45 (7), 772–777.
Kanchana, P., Sekar, C., 2015. Development of electrochemical folic acid sensor based on hydroxyapatite nanoparticles. Spectrochim. Acta Mol. Biomol. Spectrosc. 137, 58–65.
Kumar, R., Rai, R., Gautam, S., De Sarkar, A., Tiwari, N., Jha, S.N., Bhattacharyya, D., Ganguli, A.K., Bagchi, V., 2017. Nano-structured hybrid molybdenum carbides/nitrides generated in situ for HER applications. J. Mater. Chem. 5 (17), 7764–7768.
Lavanya, N., Fazio, E., Neri, F., Bonavita, A., Leonardi, S., Neri, G., Sekar, C., 2016. Electrochemical sensor for simultaneous determination of ascorbic acid, uric acid and folic acid based on Mn-SnO2 nanoparticles modified glassy carbon electrode. J. Electroanal. Chem. 770, 23–32.
Li, J.-S., Wang, Y., Liu, C.-H., Li, S.-L., Wang, Y.-G., Dong, L.-Z., Dai, Z.-H., Li, Y.-F., Lan, Y.-Q., 2016. Coupled molybdenum carbide and reduced graphene oxide electrocatalysts for efficient hydrogen evolution. Nat. Commun. 7, 11204.
Liu, Y., Li, G.-D., Yuan, L., Ge, L., Ding, H., Wang, D., Zou, X., 2015. Carbon-protected bimetallic carbide nanoparticles for a highly efficient alkaline hydrogen evolution reaction. Nanoscale 7 (7), 3130–3136.
Lv, C., Huang, Z., Yang, Q., Wei, G., Chen, Z., Humphrey, M.G., Zhang, C., 2017. Ultrafast

synthesis of molybdenum carbide nanoparticles for efficient hydrogen generation. J. Mater. Chem. 5 (43), 22805–22812.
Naguib, M., Unocic, R.R., Armstrong, B.L., Nanda, J., 2015. Large-scale delamination of multi-layers transition metal carbides and carbonitrides “MXenes”. Dalton Trans. 44 (20), 9353–9358.
Ng, V.M.H., Huang, H., Zhou, K., Lee, P.S., Que, W., Xu, J.Z., Kong, L.B., 2017. Recent progress in layered transition metal carbides and/or nitrides (MXenes) and their composites: synthesis and applications. J. Mater. Chem. 5 (7), 3039–3068.
Pan, G., Shinde, S., Yeung, S.Y., Jakštaitė, M., Li, Q., Wingren, A.G., Sellergren, B., 2017a. An epitope-imprinted biointerface with dynamic bioactivity for modulating cell–-biomaterial interactions. Angew. Chem. Int. Ed. 56 (50), 15959–15963.
Pan, Y.-X., Peng, J.-B., Xin, S., You, Y., Men, Y.-L., Zhang, F., Duan, M.-Y., Cui, Y., Sun, Z.-Q., Song, J., 2017b. Enhanced visible-light-driven photocatalytic H2 evolution from water on noble-metal-free CdS-nanoparticle-dispersed Mo2C@ C nanospheres. ACS Sustain. Chem. Eng. 5 (6), 5449–5456.
Piletsky, S.A., Turner, N.W., Laitenberger, P., 2006. Molecularly imprinted polymers in clinical diagnostics—future potential and existing problems. Med. Eng. Phys. 28 (10), 971–977.
Pu, Z., Wang, M., Kou, Z., Amiinu, I.S., Mu, S., 2016. Mo 2 C quantum dot embedded chitosan-derived nitrogen-doped carbon for efficient hydrogen evolution in a broad pH range. Chem. Commun. 52 (86), 12753–12756.
Qamar, M., Adam, A., Merzougui, B., Helal, A., Abdulhamid, O., Siddiqui, M., 2016. Metal–organic framework-guided growth of Mo 2 C embedded in mesoporous carbon as a high-performance and stable electrocatalyst for the hydrogen evolution reaction. J. Mater. Chem. 4 (41), 16225–16232.
Tang, C., Sun, A., Xu, Y., Wu, Z., Wang, D., 2015a. High specific surface area Mo2C nanoparticles as an efficient electrocatalyst for hydrogen evolution. J. Power Sources 296, 18–22.
Tang, C., Wang, W., Sun, A., Qi, C., Zhang, D., Wu, Z., Wang, D., 2015b. Sulfur-decorated molybdenum carbide catalysts for enhanced hydrogen evolution. ACS Catal. 5 (11), 6956–6963.
Wang, D., Wang, J., Luo, X., Wu, Z., Ye, L., 2017. In situ preparation of Mo2C nanoparticles embedded in Ketjenblack carbon as highly efficient electrocatalysts for hydrogen evolution. ACS Sustain. Chem. Eng. 6 (1), 983–990.
Xiao, Y., Hwang, J.-Y., Sun, Y.-K., 2016. Transition metal carbide-based materials: synthesis and applications in electrochemical energy storage. J. Mater. Chem. 4 (27), 10379–10393.
Xiong, K., Lee, W.S., Bhan, A., Chen, J.G., 2014. Molybdenum carbide as a highly selective deoxygenation catalyst for converting furfural to 2-methylfuran. ChemSusChem 7 (8), 2146–2149.
Xu, C., Wang, L., Liu, Z., Chen, L., Guo, J., Kang, N., Ma, X.-L., Cheng, H.-M., Ren, W., 2015. Large-area high-quality 2D ultrathin Mo 2 C superconducting crystals. Nat. Mater. 14 (11), 1135.
Yuan, W., Cheng, L., Wu, H., Zhang, Y., Lv, S., Guo, X., 2018. One-step synthesis of 2D-layered carbon wrapped transition metal nitrides from transition metal carbides (MXenes) for supercapacitors with ultrahigh cycling stability. Chem. Commun. 54 (22), 2755–2758.
Zaidi, S.A., 2013. Dual-templates molecularly imprinted monolithic columns for the evaluation of serotonin and histamine in CEC. Electrophoresis 34 (9–10), 1375–1382.
Zaidi, S.A., 2016. Latest trends in molecular imprinted polymer based drug delivery systems. RSC Adv. 6 (91), 88807–88819.
Zaidi, S.A., 2017. Molecular imprinting polymers and their composites: a promising material for diverse applications. Biomater. Sci. 5 (3), 388–402.
Zaidi, S.A., 2018. Utilization of an environmentally-friendly monomer for an efficient and sustainable adrenaline imprinted electrochemical sensor using graphene. Electrochim. Acta 274, 370–377.
Zaidi, S.A., Lee, S.M., Cheong, W.J., 2011. Open tubular capillary columns with basic templates made by the generalized preparation protocol in capillary electrochromatography chiral separation and template structural effects on chiral separation capability. J. Chromatogr. A 1218 (9), 1291–1299.
Zhai, Q., Zhang, X., Li, J., Wang, E., 2016. Molybdenum carbide nanotubes: a novel multifunctional material for label-free electrochemical immunosensing. Nanoscale 8 (33), 15303–15308.
Zhang, H.J., Wang, K.X., Wu, X.Y., Jiang, Y.M., Zhai, Y.B., Wang, C., Wei, X., Chen, J.S., 2014. MoO2/Mo2C heteronanotubes function as high-performance Li-ion battery electrode. Adv. Funct. Mater. 24 (22), 3399–3404.
Zhu, J., Sakaushi, K., Clavel, G., Shalom, M., Antonietti, M., Fellinger, T.-P., 2015. A general salt-templating method to fabricate vertically aligned graphitic carbon nanosheets and their metal carbide hybrids for superior lithium ion batteries and water splitting. J. Am. Chem. Soc. 137 (16), 5480–5485.